Carbon Capture Science & Technology 14 (2025) 100382

Contents lists available at ScienceDirect

Carbon Capture Science & Technology

journal homepage: www.elsevier.com/locate/ccst

Full Length Article

Pyrolysis-catalytic gasification of plastic waste for hydrogen-rich syngas production with hybrid-functional Ni-CaO–Ca_2SiO_4 catalyst

Tian Heng Qin[a], Guozhao Ji[b], Boyu Qu[a,b], Alan J McCue[c], Shaoliang Guan[d], Jos Derksen[a], Ye Shui Zhang[a,*]

[a] School of Engineering, University of Aberdeen, Aberdeen AB24 3UE, UK
[b] Key Laboratory of Industrial Ecology and Environmental Engineering, School of Environmental Science & Technology, Dalian University of Technology, Dalian 116024, China
[c] Advanced Centre for Energy and Sustainability (ACES), Department of Chemistry, School of Natural and Computing Sciences, University of Aberdeen, Aberdeen, AB24 3UE, UK
[d] Department of Materials Science and Metallurgy, University of Cambridge, Cambridge, CB3 0FS, UK

ARTICLE INFO

Keywords:
Pyrolysis-catalytic gasification
Hydrogen
Plastic waste
Hybrid-functional catalyst

ABSTRACT

The production of H_2-rich syngas from pyrolysis-catalytic gasification of plastic waste bottles has been investigated. The hybrid-functional materials consisting of Ni as catalyst, CaO as CO_2 sorbent and Ca_2SiO_4 as a polymorphic active spacer were synthesized. The different parameters (Ni loading, temperature, N_2 flow rate and feedstock-to-catalyst ratio) have been investigated to optimise the H_2 production. The catalysts were analysed by N_2 physisorption, scanning electron microscopy (SEM), energy dispersive spectroscopy (EDS), X-ray diffraction (XRD), X-ray photoelectron spectroscopy (XPS), Temperature-programmed reduction (TPR) and *in-situ* Transmission Electron Microscopy (TEM). Temperature-programmed oxidation (TPO) was used to analyse the carbon formation on the used catalysts. The highest H_2 production of 59.15 mmol $g^{-1}_{\text{of plastic}}$ was obtained in the presence of a catalyst with 20 wt.% Ni loading, which amounts to H_2 purity as high as 54.2 vol% in gas production. Furthermore, 90.63 mmol $g^{-1}_{\text{of plastic}}$ of syngas was produced by increasing the feedstock-to-catalyst ratio to 4:1, yielding 84.4 vol.% of total gas product (53.1 vol.% of H_2 and 31.3 vol.% of CO, respectively). The Ni-CaO–Ca_2SiO_4 hybrid-functional material is a very promising catalyst in the pyrolysis-catalytic gasification process by capturing CO_2 as it is produced, therefore shifting the water gas shift (WGS) reaction to enhance H_2 production from plastic waste. Detailed elucidation of the roles of each component at the microscale during the catalytic process was also provided through *in-situ* TEM analysis. The finding could guide the industry for future large-scale application to convert abundant plastic waste into H_2-rich syngas, therefore contributing to the global 'net zero' ambition.

1. Introduction

Hydrogen (H_2) is considered as an environmental-friendly fuel that has the potential to reduce the world consumption of fossil fuels to meet sustainable development goals. The demand for H_2 reached 97 million tons (Mt) in 2023, of which <1 % was low emissions. Based on announced projects, low-emissions H_2 could reach 49 Mtpa by 2030 (Wu et al., 2019; Dawood et al., 2020; Nnabuife et al., 2022; IEA 2024). In 2023, >80 % of H_2 produced annually was from unabated fossil fuel and coal feedstocks, resulting in no discernible impact on climate change mitigation. Over the past two years, the production of low-emissions H_2 equipped with carbon capture, utilization, and storage (CCUS) technologies has seen slight growth, still remaining below 1 Mtpa H_2, which constitutes <1 % of global hydrogen output (Antonini et al., 2020; Khan et al., 2021). H_2 production from thermo-chemical process has received growing attention due to the flexibility of handling various feedstocks (Ji et al., 2017; Zhang and Williams, 2016), especially from renewable biomass and solid wastes. Another benefit is the possibility to produce high-valued carbon materials like carbon nanotubes (CNTs) at the same time (Zhang and Williams, 2016; Zhang et al., 2017; Zhang et al., 2015; Xu et al., 2023; Liu et al., 2023). More than 90 % of plastic production relies on fossil fuels. The global plastic production reached 413.8 Mt in 2023, meanwhile 374.2 Mt plastic were fossil-based (Nielsen et al., 2020; IEA 2024). In the same year, only lower than 0.1 % of plastic was chemical recycled or carbon-captured. Considering it mostly consists with carbon and hydrogen, waste plastic could be an ideal feedstock for H_2 production and CCUS. Polyethylene terephthalate (PET) is a thermoplastic polymer widely utilized in both industry

* Corresponding author.
E-mail address: yeshui.zhang@abdn.ac.uk (Y.S. Zhang).

https://doi.org/10.1016/j.ccst.2025.100382
Received 26 October 2024; Received in revised form 15 January 2025; Accepted 28 January 2025

and daily life. Its significant resistance to natural decomposition and widespread use in single-use packaging underscores its considerable environmental impact, which caused massive pollution in both land and marine systems (Tournier et al., 2020; Villarrubia-Gómez et al., 2022; MacLeod et al., 2021). It has been predicted that the global PET plastic recycling market reach USD 10.548 billion in 2024, growing at a compound annual growth rate (CAGR) of 7.00 % from 2024 to 2031 (Phagare, 2024).

Gasification is a thermo-chemical conversion process that holds paramount significance in the realm of sustainable energy production and waste management, typically carried out in the presence of pure oxygen, air or steam at temperatures in the range 700 - 950 ˚C under atmospheric pressure (Lopez et al., 2018). For highly contaminated waste or unsorted plastic waste, gasification is considered as one of the most promising technologies (Heidenreich and Foscolo, 2015; Sikarwar et al., 2017; Ranzi et al., 2001; Dogu et al., 2021; Ciuffi et al., 2020). The introduction of low-cost steam into plastic waste gasification can yield H_2 and enhance the WGS simultaneously. Two-stage processes have been widely employed for pyrolysis-catalytic gasification of plastic waste by many researchers (Zhang et al., 2017; Zhang et al., 2022; Wu and Williams, 2009; Zhang et al., 2017). Plastic waste is firstly pyrolyzed to decompose the solid feedstock into volatiles in the first stage, then the volatiles will be sent to a second-stage for syngas production. The temperature in the second catalytic stage is usually higher than the pyrolysis stage, which catalyse the process of steam reforming and generation of H_2 (Zou et al., 2021).

Catalysis plays a pivotal role in enhancing H_2 productivity. Although noble metals perform efficiently in increasing H_2 yield, their high price means they are not ideal for use at an industrial scale (Williams, 2021). Transition metals such as nickel, iron and cobalt have been widely used for hydrocarbon reforming in thermo-chemical conversion processes (Zhang et al., 2021). For example, Liu et al. (2023) developed rose-like $Co_xMn_{3-x}O_4$ spinel smart pre-catalysts that can self-convert into the targeted active site-rich Co/MnO catalysts for the high-efficiency conversion of plastic waste. Zhang et al. (2017) used mesoporous MCM-41 supported Fe and Ni bimetallic catalysts for H_2-rich syngas production from a mixture of plastic waste. Xu et al. (2023) proposed advanced bimetallic NiCo/MnO catalysts for H_2 production from waste polypropylene via a molecular- and macroscale-level engineering strategy. Density functional theory (DFT) simulations then rationalized the activity of NiCo/MnO catalysts in the dehydrogenation of hydrocarbons. Xu et al. (2022) also reported catalytic degradation of plastic wastes with typical fluid catalytic cracking catalyst (FCC). The yield and composition of liquid and gas products over various FCCs were studied quantitatively.

Nickel has been identified as one of the most efficient catalysts in cracking C–C, C–H and C–O bonds, which are the main chemical bonds within plastics (Ji et al., 2017; Zhang et al., 2017; Xu et al., 2023; Chai et al., 2020). Ni-based materials are commonly utilised catalysts for the commercial production of H_2 due to high thermal stability and selectivity to H_2, although it also demonstrates high reactivity in promoting the water gas shift reaction (Davda et al., 2005; Chen and Chen, 2020, González-Castaño et al., 2021). Therefore, even the most challenge tar cracking and light hydrocarbon reforming during plastic pyrolysis-gasification could be achieved (Wu et al., 2019; Hu et al., 2018; Zhang et al., 2019). As nickel oxide (NiO) could be reduced to nickel during the process and still give high H_2 yield, it is acceptable to have no reduction pre-treatment before use. Different from analytical grade chemicals, waste calcium materials possess great potential to be used with fairly low cost. It is reported that calcium oxide (CaO) can facilitate tar cracking and catalyse cracking/gasification, which has been widely used for capturing CO_2 due to its high sorption capacity (Li et al., 2021; Wu et al., 2024; Wang et al., 2021; Wang et al., 2022; Zhou et al., 2024). Since CO_2 is produced along with H_2 during the steam reforming of plastic waste, it is feasible to capture CO_2 as its formed during the reaction process and shift the equilibrium of reversible reactions for more H_2 and CO yield. Ca_2SiO_4 has been reported to show reversible polymorphic transitions in regenerating declining porosity after reaction, as well as its strong resistance to particle sintering (Ji et al., 2017). As previously reported (Ji et al., 2017), Ni-CaO catalyst without Ca_2SiO_4 even gives higher hydrogen yield compared to Ni-Ca_2SiO_4_CaO or Ni-Ca_2SiO_4. However, using calcium oxide as a catalyst support alone will easily lead to problems such as catalyst skeleton collapse and nickel sintering. After 15 cycles of reaction, the hydrogen yield of Ni-CaO decreased remarkably while hydrogen production for Ni-Ca_2SiO_4_CaO was reduced only slightly.

In this work, a Ni-CaO–Ca_2SiO_4 hybrid-functional material has been prepared to investigate its performance for pyrolysis-catalytic gasification of plastic waste for H_2-rich syngas production at different conditions. NiO plays the role of activation centre of the catalyst, which is reduced during the reaction process to the more active metallic state. CaO acts as a CO_2 sorbent and Ca_2SiO_4 functions as a stabilizer/anti-agglomeration agent in waste PET steam gasification. Real world plastic waste bottles were used as feedstock. This study aims to optimize the process for H_2 and syngas production in the presence of Ni-CaO–Ca_2SiO_4 hybrid-functional materials as catalyst with a two-stage fixed-bed reactor. Different parameters have been studied, including carrier gas flow rate, catalytic temperature, Ni loading and feedstock-to-catalyst ratio.

2. Materials and methods

2.1. Sample preparation

All chemicals used in this research were purchased from Sigma-Aldrich, U.K with purity over 99 %. 5 mmol tetraethyl orthosilicate (TEOS, $Si(OC_2H_5)_4$) was dissolved into 500 mL 1 mmol L^{-1} nitric acid (HNO_3) and stirred at 600 r min^{-1} at room temperature (RT) for 45 min. Then 45 mmol calcium acetate (PhosLo gelcaps) hydrate ($Ca(C_2H_3O_2)_2$) and nickel (II) nitrate hexahydrate ($Ni(NO_3)_2{\cdot}6H_2O$) were added to the solution after TEOS was completely hydrolysed. After the precursor became homogeneous, it was dried at 95 ˚C in an oven overnight. The same procedure was repeated but with varying the Ni content (5 wt.%, 10 wt.%, 15 wt.%, 20 wt.%) to analyse the influence of Ni loading by keeping the CaO:Ca_2SiO_4 ratio consistent at 3:7. The calculations were based on a published work from Ji et al. (2017). These samples were denoted as Ni05, Ni10, Ni15 and Ni20, respectively. All the dried precursors were calcined at 850 ˚C (ramping rate 5 ˚C min^{-1}) for 1 h in air. The catalyst sample was then ground and sieved to a size between 50 and 180 μm before experiment and characterization. Washed Coca Cola bottles (500 mL) were cut into small fragments (15 × 3 mm) as feedstock. The lid and label were not used in this work. The proximate analysis of the Coca Cola bottles was obtained from SOCOTEC, UK and was given in Table 1.

2.2. Experimental system

Experiments were undertaken using a two-stage fixed-bed reactor for pyrolysis–catalytic gasification experiments (Zhang et al., 2015; Zhang et al., 2022). The 3D model of the reactor tube and schematic diagram of the reactor are shown in Fig. 1. The reactor was constructed of S316 stainless steel and was externally heated with a multi zone furnace with full temperature control and monitoring. Pyrolysis of the plas-

Table 1
Proximate analysis of the Coca Cola bottle (as received).

Moisture content (wt.% wet basis)	0.4
Ash content (wt.% wet basis)	< 0.1
Elemental analysis (wt.% dry basis)	
C	62.61
H	4.18
O	33.19
N	< 0.05
S	< 0.02

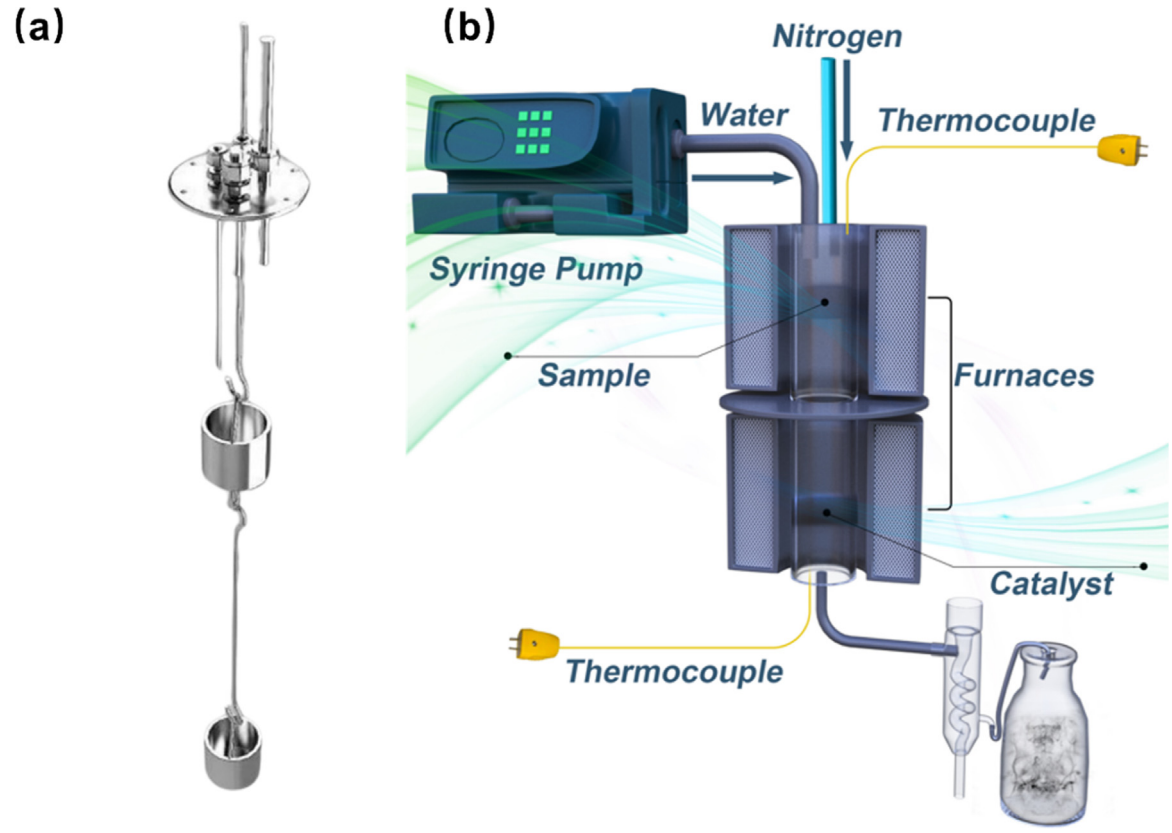

Fig. 1. (a) 3D model of the reactor tube, plastic feedstock and catalysts are placed in the upper and lower crucibles, respectively; (b) Schematic diagram of the two-stage fixed-bed reactor (Zhang et al., 2022). Reprinted (adapted) with permission from (Zhang et al., 2022) © (2022) American Chemistry Society.

tic waste occurred in the first/top stage at 600 °C, and the produced volatiles were passed directly to the second/bottom stage, where catalytic reactions occurred at 700, 800 or 900 °C. Nitrogen (N_2) was introduced into the process from the top of the pyrolysis reactor as the inert purge gas with a flow rate of 80, 110 or 140 mL min^{-1}. The plastic bottle sample (0.5 g) was placed in the top stage, and the catalyst (0.5 g) was placed in the bottom stage. Quartz wool (around 0.7 g) was used to spread out the catalyst. During the experiments, the catalyst bed (second stage) was preheated to the targeted temperature. Then, the pyrolysis stage started heating from RT to 600 °C with a heating rate of 40 °C min^{-1}. Water injection was introduced into the second stage of the process via a syringe pump with a flow rate of 5 mL h^{-1}. Heating of the top pyrolysis stage, water injection and gas collection started at the same time. The gaseous products from the process were passed to a condensation system to trap the condensable liquids, followed by gas collection in a 12 L Tedlar® gas sampling bag. The cracking of plastic waste took around 40 min, and the gas collection time was around 60 min (extra time was used to ensure that all products are collected).

2.3. Analytical methods

The gaseous products were collected by the Tedlar® gas sampling bag and analysed with gas chromatography (GC) with a Thermal conductivity detector (TCD) using a capillary column (30 m × 0.25 mm, Thermo Scientific TraceGOLD^{TM} TG-WaxMS A) (Silva and Dionisi, 2020).

The used catalysts were analysed by temperature programme oxidation (TPO) using a thermogravimetric analyser (TGA) (Mettler Toledo TGA/DSC 3 + system) to determine the oxidation characteristics of carbon deposited on the catalyst. Each used catalyst sample was placed in the TGA and heated in air at a flow rate of 20 mL min^{-1} to 900 °C at a heating rate of 15 °C min^{-1}. All the samples were held for 10 mins at 120 °C to remove the moisture.

The porous properties of the catalysts were determined by obtaining the N_2 adsorption and desorption isotherms at equilibrium vapour pressure using the static volumetric method. N_2 adsorption–desorption isotherms were recorded at −196 °C using a TriStar II Plus instrument (Micromeritics). The samples were degassed at 300 °C for 4 h prior to analysis. Specific surface areas were determined according to the Brunauer, Emmett and Teller (BET) model, with pore diameters, volumes and size distributions determined through Barrett-Joyner-Halenda (BJH) desorption analysis.

The crystalline structure and chemical phase composition of the fresh catalyst was assessed by X-ray diffraction (XRD) analysis with a PANalytical X'Pert X-ray Powder diffractometer (PIXcel 1D detector) (D/Max 2500 V+/PC, Cu Kα, 2θ = 10–90°, step interval = 0.02°).The fresh and spent catalysts were characterized by scanning electron microscopy (SEM) (Zeiss GeminiSEM 300) to determine surface morphologies of the catalyst particles. The element distributions of fresh catalysts were explored with energy-dispersive X-ray spectroscopy (EDS) associated with the SEM.

Temperature Programmed Reduction (TPR) experiments on fresh oxidised catalysts were conducted to characterize the metal surface of the catalyst and investigate the optimal reduction conditions. A TPDRO 1100 instrument was used with a TCD detector, with a trap bed placed before the detector to remove the moisture. Samples were firstly dried by increasing the temperature up to 105 °C for 30 min under N_2 flow, then the system was cooled down and the temperature was increased again until 1000 °C with a 6 °C min^{-1} temperature ramp, using a 5 % H_2/N_2 flow.XPS Analysis was performed using a Thermo NEXSA G2 XPS fitted with a monochromated Al Kα X-ray source (1486.7 eV), a spherical sector analyser and 3 multichannel resistive plate, 128 channel delay line detectors. All data was recorded at 19.2 W and an X-ray beam size

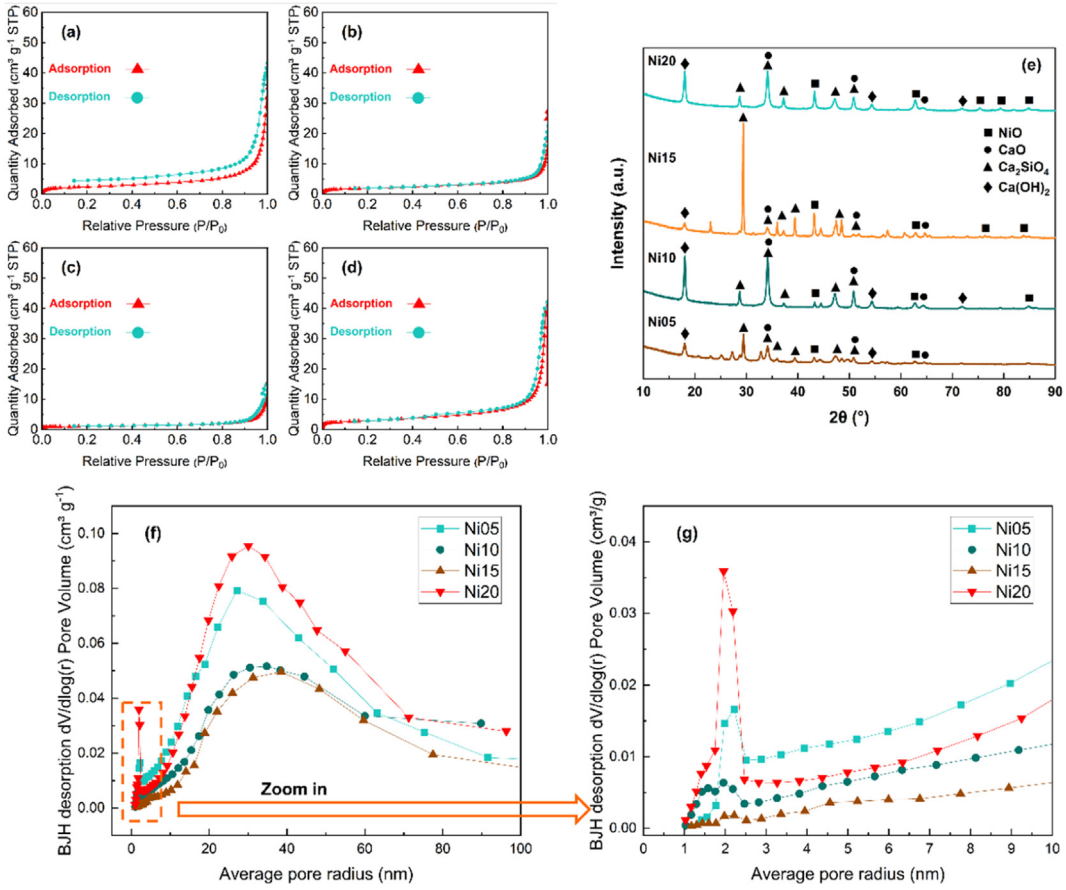

Fig. 2. N_2 adsorption isotherms of tri-functional material with various Ni loading (a) Ni05, (b) Ni10, (c) Ni15, (d) Ni20 (e). XRD patterns of all catalysts with different Ni loadings. (f). Pore volume distribution of various Ni loading catalysts (Ni05, Ni10, Ni15 and Ni20) by BJH desorption; (g) zoom in of the first peak in (f).

of 400 × 200 μm. Survey scans were recorded at a pass energy of 200 eV, and high-resolution scans recorded at a pass energy of 50 eV. Electronic charge neutralization was achieved using an ion source (Thermo Scientific FG-03). Ion gun current = 150 μA. Ion gun voltage = 40 V. All sample data was recorded at a pressure below 10^{-8} Torr and a RT. Data was analysed using CasaXPS v2.3.26rev1 .0N. Peaks were fit with a Shirley background prior to component analysis. Line shapes of LA (1.53,243) were used to fit components.

To reveal the morphology of the samples, high-resolution *in-situ* TEM images were obtained using a microscope (ARM300CF JEOL) at the electron Physical Sciences Imaging Centre (ePSIC) at Diamond Light Source, Oxford. An acceleration voltage of 200 kV was used, acquiring the micrographs of catalysts from RT to 900 °C The sample was mounted on the DENS heating nano-chip for capturing the micrographs.

3. Results and discussion

3.1. Characterization of fresh catalysts

The N_2 adsorption and desorption isotherms were plotted for the hybrid-functional materials with varied Ni loadings as shown in Fig. 2(a). There was no obvious relationship between Ni loading and porous morphology of the catalysts. All the catalysts presented a Type IV isotherm, which indicates mesoporous materials (Al-Ghouti and Da'ana, 2020). The pore volume distribution for all fresh catalysts was illustrated in Fig. 2(f), indicating the existence of both mesopores and macropores. Different from Ni10 and Ni15, Ni05 and Ni20 have a more obvious peak in the volume distribution curve at around 2.5 nm pore radius as shown in Fig. 2(g). Table 2 lists the textual properties obtained from N_2 adsorption and desorption measurements. The Ni20 has largest BET surface area of 10.32 m^2 g^{-1} and highest pore volume of 0.077 cm^3 g^{-1}. BET surface area decreases from 8.73 to 4.14 m^2 g^{-1} as Ni loading increased from Ni05 to Ni15 gradually. Pore volume follows the same trend as the BET surface area. Meanwhile, the average pore radius for the four fresh catalysts is similar and in the range of 24 to 31 nm. In Fig. 2(f), the mesoporous structure which influences the catalytical ability can be found from all catalysts for the average pore radii between 1 and 25 nm. Interestingly, Ni20 showed the highest BJH desorption volume, which is correlates with the best catalytic performance as shown in Table 3 - highest H_2 production of 59.15 mmol $g^{-1}_{\text{of plastic}}$ (discussed in more detail later).

In Fig. 2(e), the XRD patterns of materials with varied Ni loadings are presented with the peaks of NiO, CaO and Ca_2SiO_4 indicated, demonstrating the combination of these three components. The peaks corresponding to NiO became increasingly more evident with Ni loading increment, especially at 43°, 63° and 76° - 85° 2θ.

Fig. 3 displays the SEM images of fresh and used hybrid-functional materials with different Ni loadings. As the catalysts were sieved in a range between 50 and 180 μm, the images here present the surface morphology of several catalyst particle. All fresh catalysts Fig. 3(a)-(d) showed some regions of clustering.

Fresh Ni20 hybrid-functional material was also analysed by EDS elemental mapping to determine the nickel, calcium, and silicon locations on the sample. The bright dots in Fig. 4(a) indicate where Ni is loaded on the catalyst. In general, the Ni particles are distributed quite well with the exception some of some regions of clustering (see Fig. 4(b) and (d)). Calcium is distributed throughout all the particles as the main skeleton of the catalyst. From Fig. 4(b) and (c), it can be seen that the silicon mapping shows it accounts for a relatively low proportion of the catalyst and is most likely to exist in the form of calcium silicate (as indi-

Table 2
Surface area, pore size and pore volume of varied Ni loading materials.

Material	BET surface area ($m^2\ g^{-1}$)	Pore volume ($cm^3\ g^{-1}$)	Average pore radius (nm)
Ni05	8.73	0.062	29.6
Ni10	7.27	0.042	31.2
Ni15	4.14	0.023	24.2
Ni20	10.32	0.077	30.1

Table 3
Product yields and gas concentration from pyrolysis-catalytic gasification of plastic bottle with Ni-CaO–Ca_2SiO_4 catalysts.

	Parameters										
N_2 flow rate (mL min^{-1})	80	110	140	110	110	110	110	110	110	110	110
Temperature (°C)	900	900	900	900	900	900	800	700	900	900	900
Catalyst	Ni05	Ni05	Ni05	Ni10	Ni15	Ni20	Ni20	Ni20	Ni20	Ni20	SiO_2
Feedstock: Catalyst	1:1	1:1	1:1	1:1	1:1	1:1	1:1	1:1	2:1	4:1	1:1
	Yield & Mass balance										
Gas yield (wt. %)	20.43	23.17	23.28	17.57	21.33	21.50	17.12	10.39	21.70	29.44	16.46
Liquid yield* **(wt. %)**	74.92	71.75	72.70	80.28	76.23	76.29	81.46	88.04	77.42	69.88	82.73
Residue (wt. %)	1.09	1.34	0.45	0.19	0.34	0.26	0.18	0.09	0.23	0.04	0.23
Carbon (wt. %)	3.56	3.74	3.57	1.96	2.10	1.96	1.24	1.49	0.64	0.64	0.57
Mass balance (plastics + reacted water %)	86.60	80.60	88.65	92.33	95.65	91.12	91.23	90.06	100.62	95.99	93.94
H_2 production (mmol $g^{-1}_{of\ plastic}$)	39.01	46.39	46.20	53.54	57.25	59.15	56.41	37.16	57.26	56.97	37.46
CO production (mmol $g^{-1}_{of\ plastic}$)	17.21	15.18	20.54	25.42	22.37	18.43	14.54	3.07	29.89	33.66	16.83
Syngas production (mmol $g^{-1}_{of\ plastic}$)	56.22	61.57	66.75	78.98	79.62	77.57	70.94	40.23	87.15	90.63	54.29
Calorific value ($MJ\ m^{-3}$) (Anwar and Carroll, 2016)	12.63	12.07	12.73	13.00	11.79	11.49	11.32	10.33	13.11	13.78	13.17
	Gas concentration (vol. %, N_2 excluded)										
H_2	47.28	49.13	48.20	48.21	49.82	54.18	56.61	60.17	52.17	53.07	45.54
CO	20.86	16.07	21.43	22.87	19.46	16.88	14.59	4.97	27.24	31.35	20.44
CH_4	2.22	2.76	2.26	2.31	1.10	1.24	1.49	2.16	1.20	1.24	3.24
CO_2	29.64	32.03	28.11	26.61	29.62	27.70	27.31	32.70	19.39	14.33	30.91

* Liquid yield includes the liquid oil production and unreacted water.

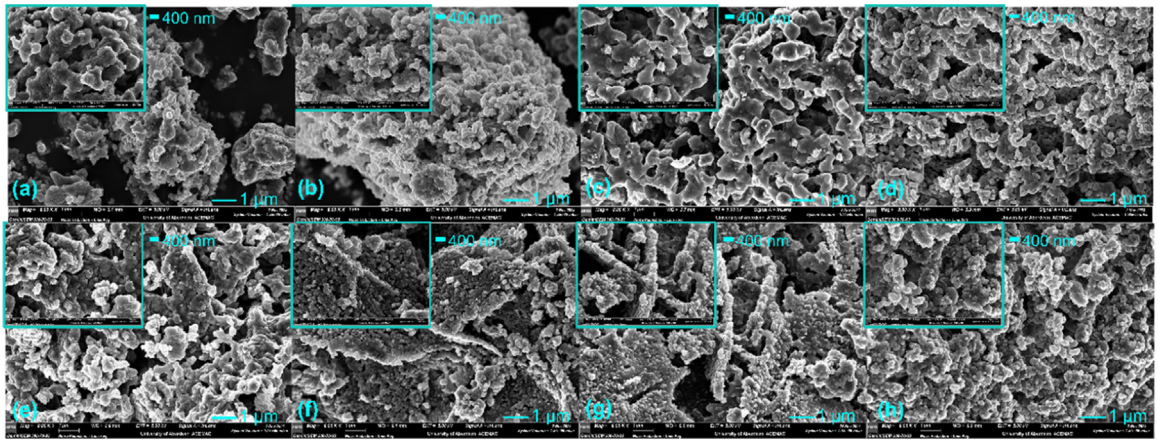

Fig. 3. SEM image of fresh hybrid-functional materials with varied Ni loadings. (a) Ni05, (b) Ni10, (c) Ni15 and (d) Ni20. SEM image of used materials. (e) Ni05, (f) Ni10, (g) Ni15, and (h) Ni20. Insets are captured at higher magnification. Reaction condition: N_2 flow rate at 110 mL min^{-1}, 900 °C, feedstock: catalyst ratio = 1:1.

cated by XRD data). The functional role being to resist particle sintering (especially CaO) during reaction.

3.2. Pyrolysis-catalytic gasification of plastic waste

Pyrolysis-catalytic gasification of the waste PET was carried out using the hybrid-functional Ni-CaO–Ca_2SiO_4 catalysts with a two-stage fixed-bed reactor. Four process parameters (Ni loading, temperature, N_2 flow rate and feedstock-to-catalyst ratio) were investigated to optimize the H_2 production with the resultant mass balance and gas concentrations shown in Table 3 and Fig. 5.

The gas product yield was calculated in relation to the initial mass of the plastic waste based on the gas concentration from GC analysis and the molecular mass of the individual gases. N_2 flow rates were precisely controlled by a mass flow controller and noted as the reference gas in Eq. (1).

The liquid yield was obtained by mass difference of the condensation system before and after experimentation. The residue was measured as the weight difference of the crucible placed in the top stage of the reactor before and after the reaction. Used catalysts were heated under air flow in TGA to quantify carbon deposition. The weight difference in the TPO curves between 200 and 900 °C is considered as the oxidation of deposited carbon with the carbon yield calculated using Eq. (2). Mass balance was calculated using the weight of products divided by the weight of the reactants (as shown in Eq. (3)). The H_2 productions were calculated based on Eq. (4).

$$Weight\ of\ gas\ (e.g.\ H_2) = \frac{gas\ concentraton\ of\ H_2}{gas\ concentration\ of\ N_2} \times \frac{gas\ collection\ time \times N_2\ flow\ rate}{ideal\ gas\ constant} \times molecular\ weight\ of\ H_2 \quad (1)$$

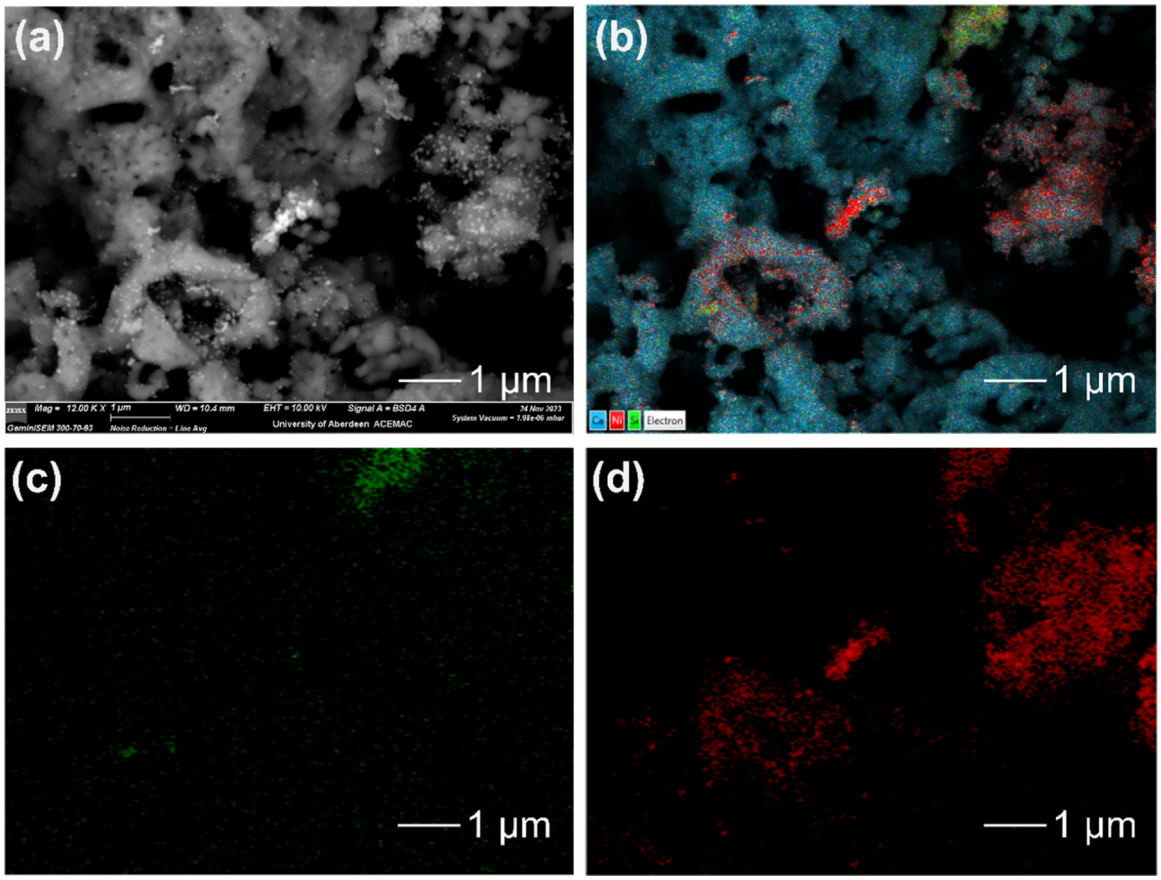

Fig. 4. EDS data for Ni20 fresh catalyst, resolution magnification at 12kX, (a) SEM image, (b) EDS layer image, indicating three different elements: calcium, nickel, and silicon, (c) EDS map of silicon, (d) EDS map of nickel.

$$Carbon\ yield\ (wt.\%) = TGA\ weight\ loss\ between\ 200-900\ ^{\circ}C\ of\ used\ catalyst \times weight\ of\ the\ used\ catalyst \quad (2)$$

$$Mass\ balance\ (\%) = \frac{weight\ of\ (gas + liquid + carbon + residue)}{weight\ of\ (plastic\ feedstock + water\ injected)} \times 100\% \quad (3)$$

$$H_2\ production\ \left(mmol^{-1}{}_{g\ of\ plastics}\right) = \frac{gas\ concentraton\ of\ H_2}{gas\ concentration\ of\ N_2} \times \frac{gas\ collection\ time \times N_2\ flow\ rate}{ideal\ gas\ constant \times weight\ of\ plastic\ feedstock} \quad (4)$$

For the pyrolysis temperature, all feedstocks were placed in the top crucible and heated to 600 °C, which is as high as is required to fully crack the plastic feedstock. Steam is introduced as a H_2 source for gasification reaction, which is similar to that reported by Zhang et al. (2015), Zhu et al. (2019) in Reaction 1 and Reaction 2. Besides, the reaction time for this experiment was always 1 hour. Considering the excessive amount of injected water, the char gasification reaction (Reaction 3) is favoured to happen on catalyst at the second stage. Therefore, three gasification temperatures (700 °C, 800 °C and 900 °C) were investigated to identify the influence of temperature on the performance of catalysts. The produced CO_2 could be captured by the CaO in the hybrid-functional catalyst (Reaction 7). CO_2 capture shift the equilibrium of water gas shift reaction (Reaction 4) and favour the H_2 production.

$$C_xH_yO_z + nH_2O \rightarrow (z+n)\ CO + (-x - z)\ C + (y/2 + n)\ H_2 \quad (R1)$$

$$C_nH_m + H_2O \rightleftharpoons nCO + (m+2)/2H_2 \quad (R2)$$

$$C + H_2O \rightarrow CO + H_2 \quad (R3)$$

$$CO + H_2O \rightleftharpoons CO_2 + H_2 \quad (R4)$$

$$C + 2H_2 \rightarrow CH_4 \quad (R5)$$

$$CH_4 + H_2O \rightleftharpoons CO + 3H_2 \quad (R6)$$

$$CaO + CO_2 \rightleftharpoons CaCO_3 \quad (R7)$$

As shown in Table 3 and Fig. 5, three N_2 flow rates (80, 110 and 140 mL min^{-1}) were investigated. The best results in Table 3 turned out to be when the N_2 flow rate was set at 110 mL min^{-1}, as the highest yield of H_2 was obtained. Specifically, the syngas production increased from 56.22 to 66.75 mmol $g^{-1}{}_{of\ plastic}$ by increasing N_2 flow rate from 80 to 140 mL min^{-1}, while the H_2 production increased from 39.01 to 46.2 mmol $g^{-1}{}_{of\ plastic}$ as shown in Fig. 5(a). The results comparing catalytic temperatures of 700, 800, and 900 °C are shown in Fig. 5(b) and Table 3. The H_2 composition declined as the rise of temperature, but syngas and H_2 productions increased remarkably, indicating higher catalytic temperature was preferred. Experiments were then conducted

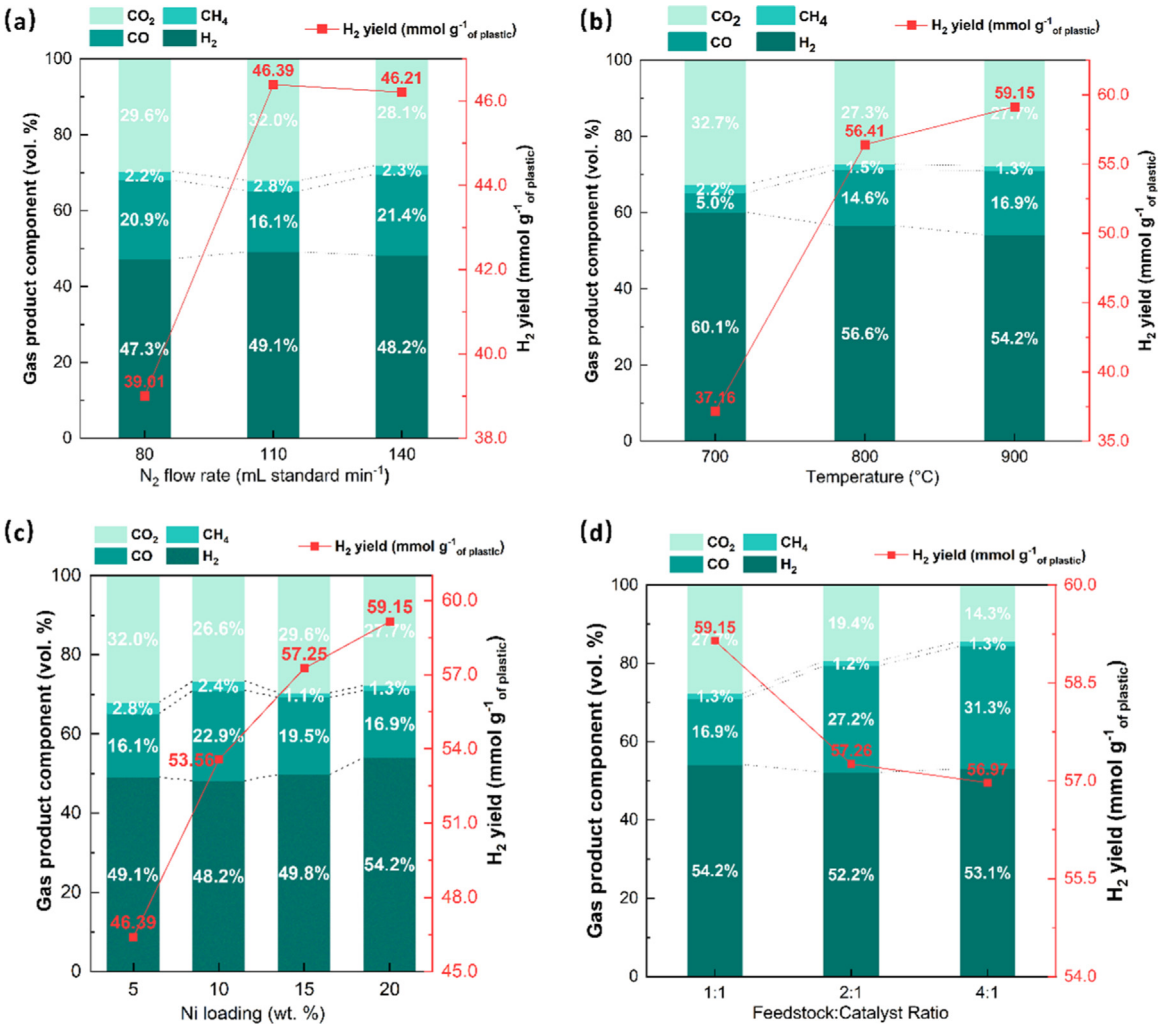

Fig. 5. Reaction process optimization column chart for gas product yield with different parameters: (a) N_2 flow rate, (b) reaction temperature, (c) Ni loading and (d) feedstock-to-catalyst ratio.

on four hybrid-functional catalysts with various Ni loading. Although the BET surface area, pore size and pore volume of those catalysts were irregular, the amount of loaded nickel showed an explicit trend. The H_2 production enhanced from 46.39 to 59.15 mmol $g^{-1}_{of\ plastic}$ as Ni loading increased from Ni05 to Ni20 in Fig. 5(c), indicating a positive correlation between Ni loading and H_2 production. The total syngas production for Ni10, Ni15 and Ni20 was around 78 mmol $g^{-1}_{of\ plastic}$ with minor deviations as shown in Table 3.

The performance of the hybrid-functional material with different feedstock-to-catalyst ratios (1:1, 2:1, 4:1) were also investigated with the best performing Ni20 catalyst. As shown in Fig. 5(d), H_2 yield reduced from 59.15 to 56.97 mmol $g^{-1}_{of\ plastic}$ when the feedstock-to-catalyst ratio increased from 1:1 to 4:1. Syngas production was increased from 77.57 to 90.63 mmol $g^{-1}_{of\ plastic}$ as shown in Table 3. It is worth pointing out that the CO_2 composition was between 26.61 to 32.70 vol. % at the feedstock-to-catalyst ratio was 1:1 where the oxygen atoms are suggested to come from PET itself and water. As shown in Fig. 5(d), when the feedstock-to-catalyst ratio augmented from 1:1 to 2:1 and 4:1, CO_2 was diminished from 27.7 to 19.4 and 14.3 vol.% respectively, consequently resulting in the elevation of CO formation from 16.9, 27.2 and 31.3 vol.%. This conversion strongly raised the total volume of syngas and reduces greenhouse gas emission from the process even under a higher feedstock-to-catalyst ratio, providing a potential for future large-scale application to convert problematic plastic waste

There was small amount of methane (CH_4) that was formed from the gasification of plastic waste or the product of the methanation reaction (Reaction 5). As shown in Fig. 5(b), the CH_4 yield decreased from 2.2 to 1.3 vol.% as the temperature rose from 700 to 900 °C. It was also influenced by the Ni loading with CH_4 yield reducing from 2.8 to 1.3 vol.% as the Ni loading increased from Ni05 to Ni20. It is suggested that the steam methane reforming (Reaction 6) was the main limitation for this, which efficiently converted CH_4 to CO and H_2. A baseline experiment was also conducted to determine the influence of Ni loading and $CaO–Ca_2SiO_4$ supported structure by replacing the support with silica-alumina (SiO_2-Al_2O_3). As shown in Table 3, the H_2 yield was as low as 37.46 mmol $g^{-1}_{of\ plastic}$ with N_2 flow rate of 110 mL min^{-1}, gasification temperature at 900 °C and feedstock-to-catalyst ratio of 1:1. The CO_2 composition (30.91 vol.%) was also very high compared with other experiments conducted in the presence of the hybrid-functional catalysts. This result strongly suggests that the CO_2 capturing ability of the hybrid catalyst (Reaction 7) shifts the equilibrium of the water gas shift reaction (Reaction 4) and thus enhanced H_2 production.

Fig. 6 shows the TPO results of used catalysts collected from all pyrolysis-catalytic gasification experiments at different conditions and aims to compare the thermal stability of the different types of carbon deposited on the catalyst. The insets are derivative thermogravimetric temperature programmed oxidation (DTG–TPO) results. The carbon with a high degree of graphitization would have a high thermal stability and tend to be combusted at higher temperatures compared

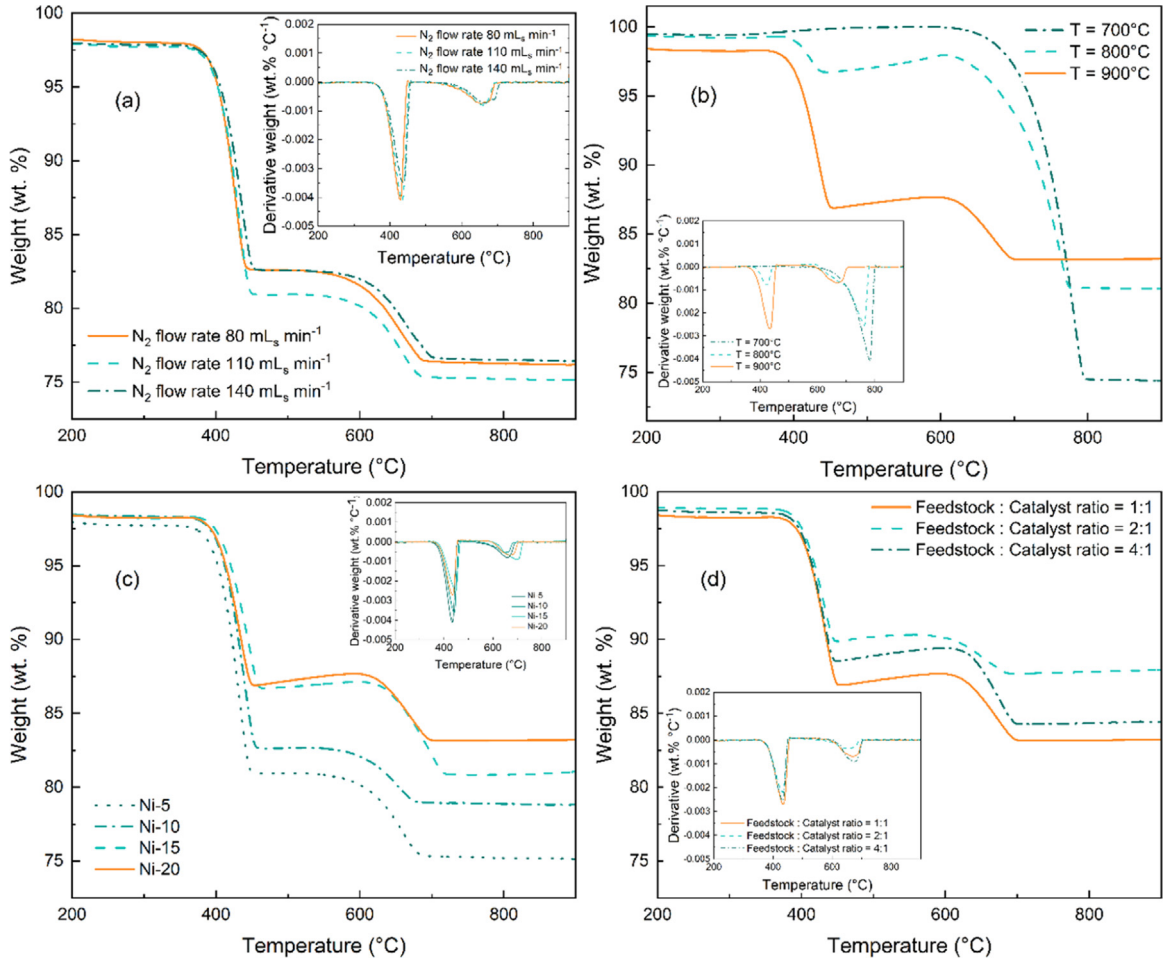

Fig. 6. TPO results of various used catalysts with different parameters, (a) N_2 flow rate, (b) reaction temperature, (c) Ni loading and (d) feedstock-to-catalyst ratio. Insets are the corresponding DTG-TPO results.

with less graphitized carbon. Carbon oxidized below 600 °C has been assigned to the decomposition of disordered/amorphous carbon, while the carbon oxidized above 600 °C has been attributed to the oxidation of graphitic/filamentous type carbons (Zhang et al., 2015; Wu and Williams, 2010). Except for catalytic tests at 700 °C, the DTG−TPO results of all used catalysts have two main oxidation peaks at around 450 and 675 °C respectively, demonstrating the formation of both amorphous and graphited carbon on the catalysts.

Data from the used catalysts were collected from the experiments with various N_2 flow rate as shown in Fig. 6(a). Similar DTG-TPO curves were observed as the gasification temperature and catalyst were the same. In Fig. 6(b), there was only one significant peak for the used catalyst at a gasification temperature of 700 °C, suggesting all the deposited carbon was mainly graphitic filamentous carbon. The elevation in gasification temperature led to a reduction in carbon weight percentage while simultaneously augmenting H_2 yield. This suggests a promising potential wherein higher temperatures could mitigate catalyst deactivation from carbon deposition. In Fig. 6(c), weight loss of the used catalysts decreased while more nickel was loaded, indicating less carbon was deposited on the catalyst. Different feedstock-to-catalyst ratio made no apparent change in the types of carbon deposited as shown in Fig. 6(d). Even relatively less carbon was formed when more feedstock was added to the reaction, suggesting saturation of carbon on used catalysts. Since 780 °C was the typical temperature for $CaCO_3$ decomposition while the reaction temperature was as high as 900 °C, all $CaCO_3$ changed back to CaO and CO_2 at the end of the experiments, providing reusage potential for this hybrid-functional catalyst. Furthermore, it can be found that the weight of used catalysts slightly increased from 400 to 650 °C, which may be caused bythe combustion of carbon deposits on the catalyst surface rather than significant oxidation of Ni . It is suggested that oxidation of Ni happen in the temperature range 500 to 1400 °C, which is not consistent with our TGA-TPO result of 400 °C to 650 °C. From the XPS result in Fig. 7 we can find that although the catalysts were reduced *in-situ* for catalysing the reactions, additional 30 mins for gas collection under 900 °C and steam environment oxidized the Ni again. The valence of Ni in used catalysts are almost similar to fresh catalyst which was no pre-reduced Ni^{2+}. SEM was also employed to characterise the used catalysts collected from pyrolysis-catalytic gasification of plastic waste experiments, and the micrographs are shown in Fig. 3(e-h).

XPS was used to track the reduction of Ni during experiments as shown in Fig. 7. Both spectra showed existence of Ni^{2+} and Ni^0 in fresh and used Ni20 catalysts. After the reaction, the deconvoluted data of Ni^0 2p spectra indicated a very slight increase in peak area percentage. At around 852.6 eV, area of Ni^0 in spectra expanded from 3.08 % to 3.52 %, indicating a slight reduction of Ni^{2+} to Ni^0 (Bagus et al., 2022). However, considering the fresh catalyst only contains very few amounts of Ni^0 while most of them are covered by NiO oxide film, and sight increasement of Ni^0 here lower than 10 % for used catalysts are suggested to be ignored. This finding matches the result from TGA-TPO, indicating there was no traceable Ni oxidation for used catalysts in Fig. 6. Similarly, this phenomenon also happened in Ni^0 peaks at around 856.2 eV and 858.5 eV as their peak areas from 0.22 % to 0.25 % and 0.57 % to 0.65 % respectively.

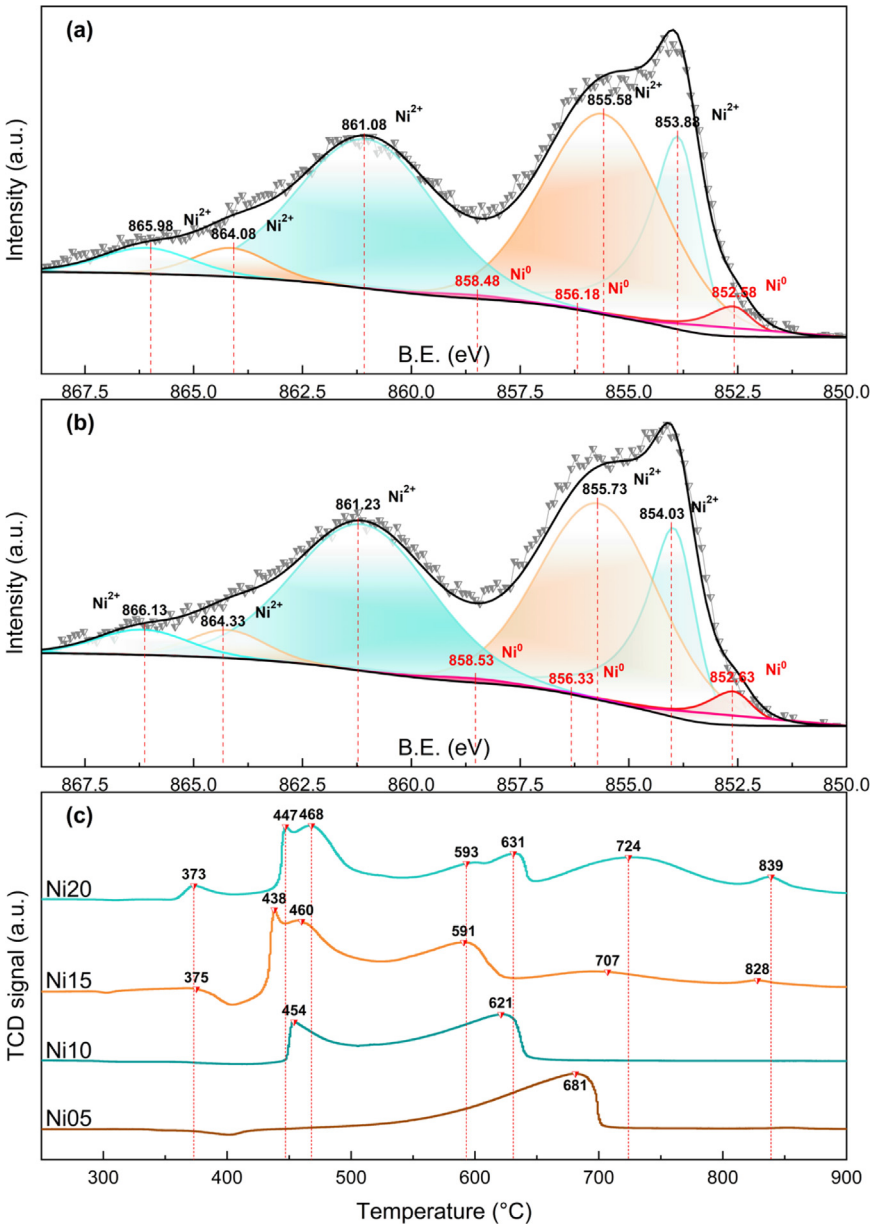

Fig. 7. XPS spectra of Ni20 catalyst (a) fresh, (b) used. Reaction conditions: N_2 flow rate at 110 mL min $^{-1}$, 900 °C, feedstock: catalyst ratio at 1:1. (c) H_2-TPR patterns for fresh catalysts with different Ni loading.

The reducibility of fresh Ni-CaO–Ca_2SiO_4 catalysts with different Ni loading was characterized by H_2-TPR and shown in Fig. 7. CaO and Ca_2SiO_4 showed no reduction peaks during the H_2-TPR test, indicating not interfere with the identification of other reducible species. Peaks around 372 °C and 450 °C becomes gradually clear as the loading of Ni increased, which are suggested to be reductive peak of free NiO to Ni (Sun et al., 2022). This kind of NiO species implies a weak interaction between catalyst support as they were reduced under a relative low temperature, which could be α-NiO (Huang et al., 2021). The broad peaks between 500 °C to 700 °C are attributed to β-NiO, indicating stronger interaction with the support (Ranjekar et al., 2023). The high-temperature peak at around 830 °C is ascribed to γ-NiO, indicating a very strong interaction with CaO or Ca_2SiO_4. This finding is consistent with the α-NiO, as γ-NiO species also demonstrated more evident peaks as Ni loading increases. Ni20 and Ni15 have all species of Ni, while Ni10 has both α-NiO and β-NiO, and Ni05 has only β-NiO respectively. From the reaction process optimization column chart in Fig. 5(c) in manuscript, it is suggested that the lack of α-NiO might be one of the reasons why Ni05 does not perform as well as other catalysts. H_2-TPR characterization also proves that all the catalysts were reduced before 900 °C during the pyrolysis/gasification reaction, ensuing there is no necessary to reduce Ni-CaO–Ca_2SiO_4 catalyst before reaction and thus more economically in potential large-scale production.

3.3. In-situ *TEM of fresh catalyst*

In-situ TEM was used to analyse the structural change of Ni20 as it is heated from RT to a catalytic temperature of 900 °C. Two kinds of typical feature were observed as shown in Fig. 8(a)/(o) and (b)/(c). Fig. 8(a) and (o) were suggested to be irregular stacking of spherical configurations, which mainly consisted of calcium salts without silicate. This component could be mostly CaO, or $Ca(OH)_2$ and $CaCO_3$ as previous literature reported (Xu et al., 2018; Ghosh et al., 2019; Sahu et al., 2023). Therefore, we propose the tentacle-like configuration observed in Fig. 8(b). (c), (d) and (e) to be Ca_2SiO_4. The portions which are in dark black colour and exhibit regular shapes could be sintered and loaded NiO depending on their size. By the observation of a tentacle-like configuration, homogeneous structures were found in Fig. 8(d), **(e),**

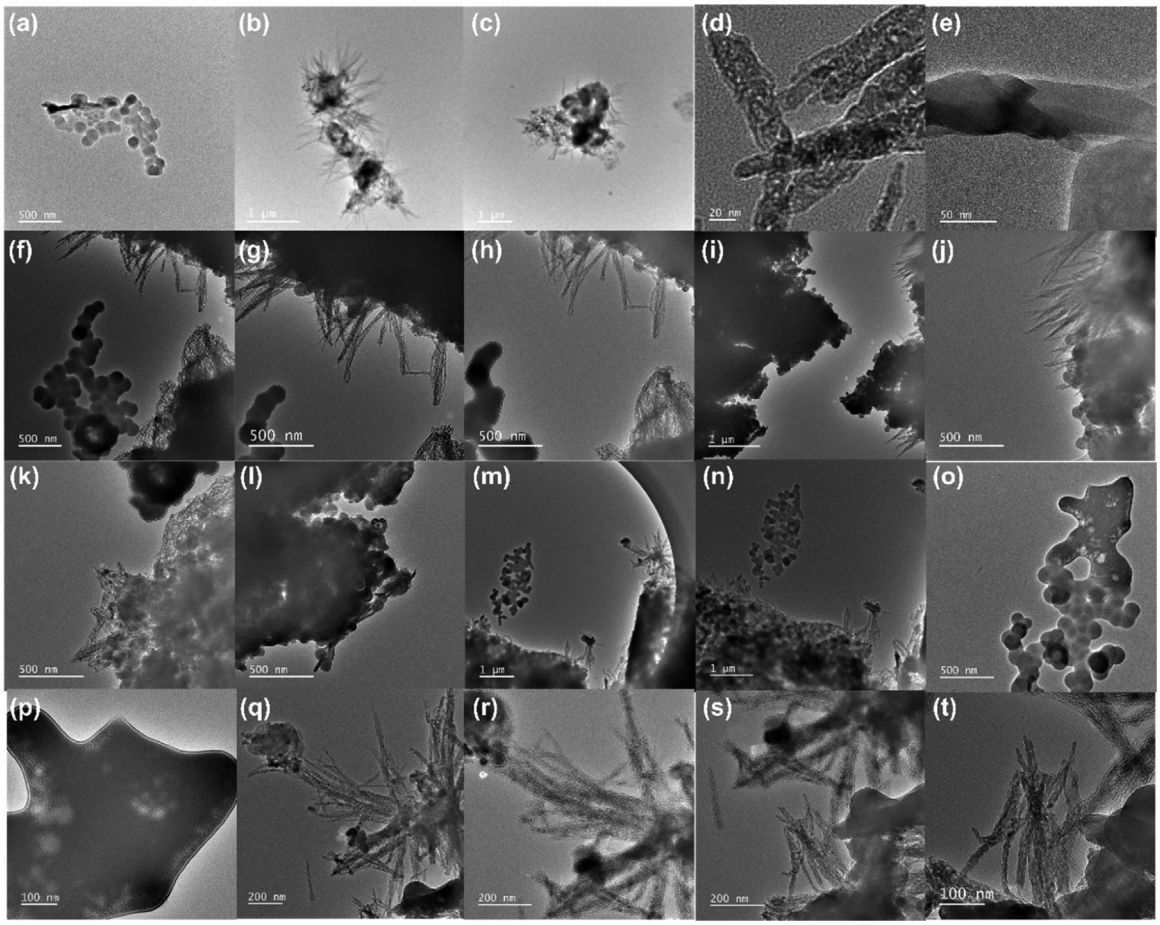

Fig. 8. TEM micrographs for different areas (a)-(t) of fresh Ni20 at RT.

(q), (r), (s) and **(t)**. The darker colour of tentacle-like configuration was caused by overlapping of those configurations, indicating that the Ca_2SiO_4 mainly plays a role in resisting sintering and enriching surface area. Two aforementioned formations can be close to each other (Fig. 8(f), (g), **(h)** and **(k)**) or combine together. The main structure of this catalyst is formed by the combination of those irregular stacking of spherical configurations and tentacle-like configurations as illustrated in Fig. 8(i), **(l), (m)** and **(n)**. The two visible characteristics of $CaO/Ca(OH)_2/CaCO_3$ and Ca_2SiO_4 were mixed to form larger aggregates of catalysts, while their properties were kept. Fig. 8(p) is the zoomed-in image of Fig. 8(o) and no spherical or tentacle-like configurations were found in this area, which could be caused by excessive overlapping of $CaO/Ca(OH)_2/CaCO_3$.

The heating of sample was progressed in stages from RT to 900 ˚C (approx. 3 ss needed for a rise of every 100 ˚C). Then the temperature was held for around 3 mins to capture TEM images. In Fig. 9, a certain area of Ni20 was observed and captured during heating up and the holding at 900 ˚C for 45 mins. It can be found that a part of amorphous black solid in the lower right corner gradually disappears from this area from 400 ˚C at Fig. 9(e), which is suggested to be the decomposition of $Ca(OH)_2$ under the vacuum environment of the TEM. The main skeleton of tentacle-like configuration remained unchanged with a rise in temperature. It is therefore suggested that there was little or no $Ca(OH)_2$ within the tentacle-like configuration of Fig. 9 as no observation of large-scale decomposition was noted in this area, which is consistent with the postulation that tentacle-like configuration was indeed Ca_2SiO_4. However, several deep black particles were found in top left and are likely NiO. Considering the decomposition temperature of $CaCO_3$ is around 825 ˚C, it can be deduced that despite the predominant presence of Ca_2SiO_4 in these tentacle-like structures, there were still residual amounts of $CaCO_3$. This hypothesis was consistent with the observation that clarity of NiO particles became more apparent at 900 ˚C from Fig. 9(j), **(k)** to **(l)**. After undergoing high-temperature process at 900 ˚C for 45 mins, the positions and shapes of these NiO particles remained virtually unchanged, maintaining an ideal distribution of these active metals. The dispersion/stability is partly attributed to the tentacle-like configuration which also demonstrated resistance at high temperatures. Moreover, no NiO particles were found loaded onto tentacle-like configuration, thus a favoured distance between NiO were kept and sintering was effectively prevented. The findings could support that the introduction of Ca_2SiO_4 offers strong resistance against particle sintering by increasing the surface area and versus porosity, therefore enables the recovery of decreased porosity after the reaction.

By comparing the same area of at RT (Fig. 8(m)) and 900 ˚C (Fig. 10(a), **(b), (c)**), the decrease of an amorphous area in the lower right corner was observed, which might be caused by the decomposition of $CaCO_3/Ca(OH)_2$. Tentacle-like configurations of Ca_2SiO_4 and spherical configurations of CaO appeared after the decomposition as shown in Fig. 10(c). However, in the comparison of the same area of Fig. 8(m), **(n)** at RT and Fig. 10(d), **(e), (f)** at 900 ˚C, no specific change was found, indicating a relative stability to carbonation /hydration in this area. Fig. 10(g) illustrated obvious spherical configurations and submicron sized pores/voids within the structure at 900 ˚C. After heating up, Fig. 8(o) was comparable with Fig. 10(h) and **(i)**. There was virtually no change to this region, suggesting a component of CaO in this area.

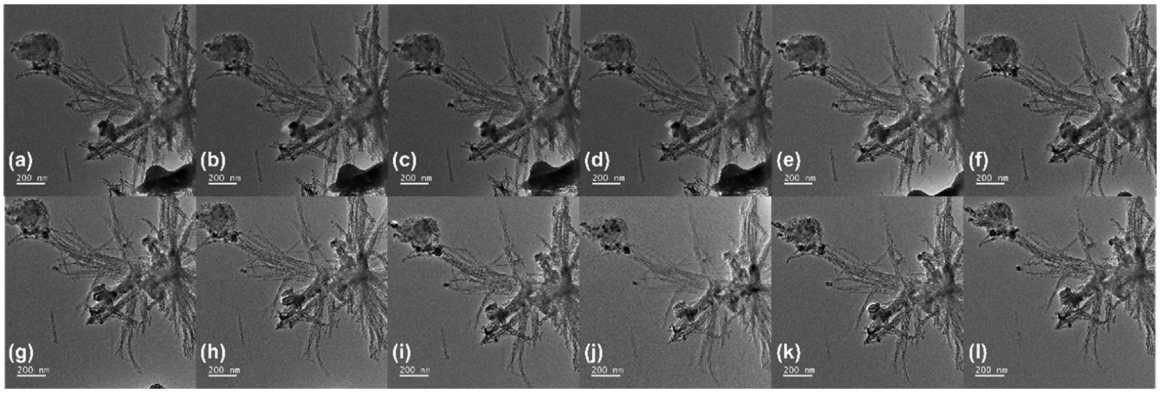

Fig. 9. *In-situ* TEM figures of fresh Ni20 during heating from RT to 900 ˚C. (a) RT, (b)100 ˚C, (c) 200 ˚C, (d) 300 ˚C, (e) 400 ˚C, (f) 500 ˚C, (g) 600 ˚C, (h) 700 ˚C, (i) 800 ˚C, (j) 900 ˚C, (k)15 mins after temperature reached 900 ˚C, (l) 45 mins after temperature reached 900 ˚C.

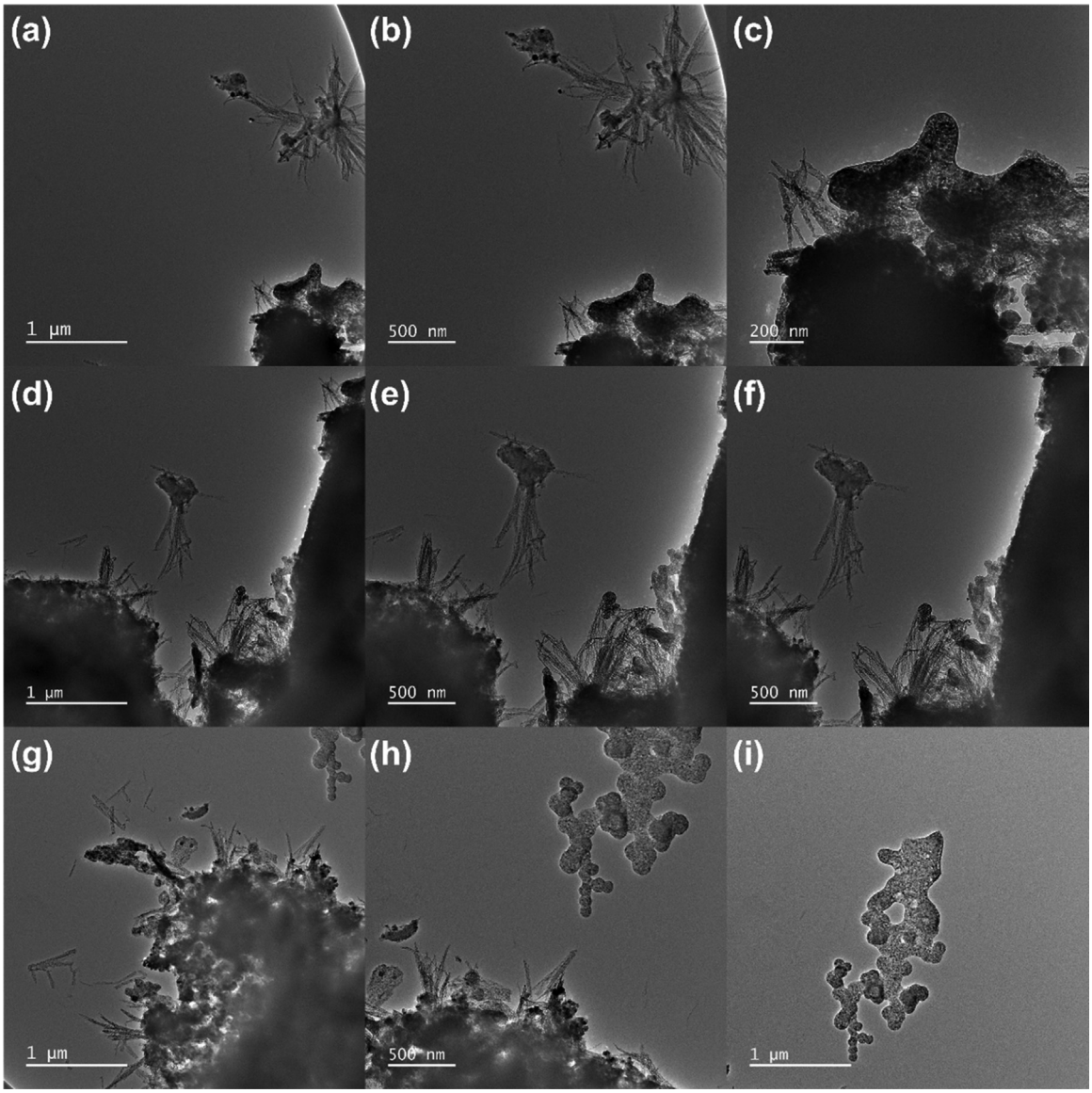

Fig. 10. TEM figures for different areas of fresh Ni20 at 900 ˚C. Resolution magnification from 15kX to 60kX. Note: the images correspond to some of the same regions imaged in Fig. 8 and this is described in depth within the text.

4. Conclusion

In this study, Ni-CaO–Ca_2SiO_4 hybrid-functional materials were prepared and investigated for the pyrolysis-catalytic gasification of PET to produce H_2-rich syngas. Four parameters (Ni loading, temperature, N_2 flow rate and feedstock-to-catalyst ratio) were investigated to optimise H_2 and syngas yields. The results suggest the following: (1) The EDS result suggests that Ni particles are distributed quite well with the exception some of some regions of clustering in the catalyst. Ni loading is the decisive factor for enhancing H_2 and syngas productions irrespective of the samples porous properties. The highest H_2 production of 59.15 mmol $g^{-1}{}_{of\ plastic}$ was obtained in presence of Ni20 catalyst with N_2 flow rate at 110 mL min^{-1}, gasification temperature at 900 °C and a feedstock-to-catalyst ratio at 1:1. (2) The gasification temperature plays a dominant role on enhancing H_2 and syngas yields, as well as the formation of the carbon. Higher temperature enhanced H_2 and syngas productions and less carbon formation. (3) Although the H_2 composition decreased as the feedstock-to-catalyst ratio increased, syngas production keeps escalating. The highest syngas production was 90.63 mmol $g^{-1}{}_{of\ plastic}$ and this was obtained with a N_2 flow rate at 110 mL min^{-1}, Ni20 as catalyst, 900 °C temperature and feedstock-to-catalyst ratio at 4:1. (4) Ca_2SiO_4 plays a significant role in resistance of catalyst sintering and formation of favoured active metal distribution. The result proves the feasibility of using the Ni-CaO–Ca_2SiO_4 hybrid-functional material for enhancing H_2-rich syngas production from plastic waste through pyrolysis-catalytic gasification process, paving a way for future large-scale application to convert problematic plastic waste into high value products, therefore contributing to the global 'net zero' ambition.

Declaration of competing interest

The authors declare that they have no known competing financial interests or personal relationships that could have appeared to influence the work reported in this paper.

CRediT authorship contribution statement

Tian Heng Qin: Writing – original draft, Visualization, Investigation, Formal analysis, Data curation. **Guozhao Ji:** Writing – review & editing, Methodology, Formal analysis, Conceptualization. **Boyu Qu:** Writing – review & editing, Formal analysis. **Alan J McCue:** Writing – review & editing, Resources, Formal analysis, Data curation. **Shaoliang Guan:** Writing – review & editing, Resources, Funding acquisition, Formal analysis, Data curation. **Jos Derksen:** Writing – review & editing, Supervision, Funding acquisition. **Ye Shui Zhang:** Writing – review & editing, Validation, Supervision, Project administration, Methodology, Funding acquisition, Formal analysis, Conceptualization.

Acknowledgement

This work was supported by the Royal Society of Chemistry Research Fund (R23-3013904115) and the Henry Royce Institute for advanced materials through the Equipment Access Scheme enabling access to the XPS at Cambridge; (Cambridge Royce facilities grant EP/P024947/1 and Sir Henry Royce Institute - recurrent grant EP/R00661X/1).

Co-funded by the European Union (HyWay:101130009). Views and opinions expressed are however those of the author(s) only and do not necessarily reflect those of the European Union or the Research Executive Agency. Neither the European Union nor the Research Executive Agency can be held responsible for them.

This work was funded by UK Research and Innovation (UKRI) under the UK government's Horizon Europe funding guarantee [EP/Y036751/1].

This work was carried out with the support of Diamond Light Source, instrument E02: a JEOL ARM300CF optimised for high resolution imaging (proposal MG35729). We extend our sincere appreciation to the dedicated support team at Diamond Light Source (Dr Mohsen Danaie and Dr Chris Allen), and the technical team at the University of Aberdeen (Jonathan Boschen-Rose, Yaroslav Kruchek and Ifeyinwa Orakwe) whose expertise and diligence have been instrumental in ensuring the success and efficiency of our operations. Their invaluable contributions are deeply acknowledged and celebrated. Special thanks are due to Mr. Chang Su from Yangzhou Yichuan Machinery Co. Ltd., P. R. China, for contributing to the 3D model design of Fig. 1(a).

References

Al-Ghouti, M.A., Da'ana, D.A., 2020. Guidelines for the use and interpretation of adsorption isotherm models: a review. J. Hazard. Mater. 393, 122383.
Antonini, C., Treyer, K., Streb, A., van der Spek, M., Bauer, C., Mazzotti, M., 2020. Hydrogen production from natural gas and biomethane with carbon capture and storage–A techno-environmental analysis. Sustain. Energy Fuels 4, 2967–2986.
Anwar, S., Carroll, J.J., 2016. Carbon Dioxide Thermodynamic Properties Handbook: Covering Temperatures from-20° to 250 °C and Pressures Up to 1000 Bar. John Wiley & Sons.
Bagus, P.S., Nelin, C.J., Brundle, C.R., Crist, B.V., Ilton, E.S., Lahiri, N., Rosso, K.M., 2022. Main and satellite features in the Ni 2p XPS of NiO. Inorg. Chem. 61, 18077–18094.
Chai, Y., Gao, N., Wang, M., Wu, C., 2020. H2 production from co-pyrolysis/gasification of waste plastics and biomass under novel catalyst Ni-CaO-C. Chem. Eng. J. 382, 122947.
Chen, W.-H., Chen, C.-Y., 2020. Water gas shift reaction for hydrogen production and carbon dioxide capture: a review. Appl. Energy 258, 114078.
Ciuffi, B., Chiaramonti, D., Rizzo, A.M., Frediani, M., Rosi, L., 2020. A critical review of SCWG in the context of available gasification technologies for plastic waste. Appl. Sci. 10, 6307.
Davda, R., Shabaker, J., Huber, G., Cortright, R., Dumesic, J.A., 2005. A review of catalytic issues and process conditions for renewable hydrogen and alkanes by aqueous-phase reforming of oxygenated hydrocarbons over supported metal catalysts. Appl. Catal. B: Environ. 56, 171–186.
Dawood, F., Anda, M., Shafiullah, G., 2020. Hydrogen production for energy: an overview. Int. J. Hydrogen. Energy 45, 3847–3869.
Dogu, O., Pelucchi, M., Van de Vijver, R., Van Steenberge, P.H., D'hooge, D.R., Cuoci, A., Mehl, M., Frassoldati, A., Faravelli, T., Van Geem, K.M., 2021. The chemistry of chemical recycling of solid plastic waste via pyrolysis and gasification: state-of-the-art, challenges, and future directions. Prog. Energy Combust. Sci. 84, 100901.
Ghosh, T., Bhaduri, S., Montemagno, C., Kumar, A., 2019. Sporosarcina pasteurii can form nanoscale calcium carbonate crystals on cell surface. PLoS. One 14, e0210339.
González-Castaño, M., Dorneanu, B., Arellano-García, H., 2021. The reverse water gas shift reaction: a process systems engineering perspective. React. Chem. Eng. 6, 954–976.
Heidenreich, S., Foscolo, P.U., 2015. New concepts in biomass gasification. Prog. Energy Combust. Sci. 46, 72–95.
Hu, M., Laghari, M., Cui, B., Xiao, B., Zhang, B., Guo, D., 2018. Catalytic cracking of biomass tar over char supported nickel catalyst. Energy 145, 228–237.
Huang, X., Mo, W., He, X., Fan, X., Ma, F., 2021. D.J.A.o. Tax, Effects of promoters on the structure, performance, and carbon deposition of Ni-Al2O3 catalysts for CO2–CH4 reforming, 6, 16381–16390.
IEA, Global Hydrogen Review 2024, (2024).
Ji, G., Xu, X., Yang, H., Zhao, X., He, X., Zhao, M., 2017. Enhanced hydrogen production from sawdust decomposition using hybrid-functional Ni-CaO-Ca2SiO4 materials. Environ. Sci. Technol. 51, 11484–11492.
Khan, M.H.A., Daiyan, R., Neal, P., Haque, N., MacGill, I., Amal, R., 2021. A framework for assessing economics of blue hydrogen production from steam methane reforming using carbon capture storage & utilisation. Int. J. Hydrogen. Energy 46, 22685–22706.
Li, H., Wang, Y., Zhou, N., Dai, L., Deng, W., Liu, C., Cheng, Y., Liu, Y., Cobb, K., Chen, P., 2021. Applications of calcium oxide–based catalysts in biomass pyrolysis/gasification–a review. J. Clean. Prod. 291, 125826.
Liu, X., Xu, D., Ding, H., Widenmeyer, M., Xie, W., Mellin, M., Qu, F., Chen, G., Zhang, Y.S., Zhang, Z., 2023. Multi-scale designed CoxMn3–xO4 spinels: smart pre-catalysts towards high-efficiency pyrolysis-catalysis recycling of waste plastics. Appl. Catal. B: Environ. 324, 122271.
Lopez, G., Artetxe, M., Amutio, M., Alvarez, J., Bilbao, J., Olazar, M., 2018. Recent advances in the gasification of waste plastics. A critical overview. Renew. Sustain. Energy Reviews 82, 576–596.
MacLeod, M., Arp, H.P.H., Tekman, M.B., Jahnke, A., 2021. The global threat from plastic pollution. Science (1979) 373, 61–65.
Nielsen, T.D., Hasselbalch, J., Holmberg, K., Stripple, J., 2020. Politics and the plastic crisis: a review throughout the plastic life cycle. Wiley Interdiscip. Rev.: Energy Environ. 9, e360.
Nnabuife, S.G., Ugbeh-Johnson, J., Okeke, N.E., Ogbonnaya, C., 2022. Present and projected developments in hydrogen production: a technological review⁎. Carbon Capture Sci. Technol. 3, 100042.
Phagare, M., 2024. PET plastic recycling Market Report 2025 (Global Edition), Cognitive Market Research, chemical & materials PET plastic recycling Market.
PlasticEurope, Plastics–the fast facts 2024, (2024).
Ranjekar, A.M., Yadav, G.D.J.I., 2023. E.C. Research, Rice husk ash-derived Ca-Mg-modified silicate as support for Ni-Co for hydrogen production by sorption-enhanced steam reforming of bioethanol, 62, 1806–1818.
Ranzi, E., Dente, M., Goldaniga, A., Bozzano, G., Faravelli, T., 2001. Lumping procedures in detailed kinetic modeling of gasification, pyrolysis, partial oxidation and combustion of hydrocarbon mixtures. Prog. Energy Combust. Sci. 27, 99–139.

Sahu, S., Saikia, K., Gurunathan, B., Dhakshinamoorthy, A., Rokhum, S.L., 2023. Green synthesis of CaO nanocatalyst using watermelon peels for biodiesel production. Mol. Catal. 547, 113342.
Sikarwar, V.S., Zhao, M., Fennell, P.S., Shah, N., Anthony, E., 2017. Progress in biofuel production from gasification. Prog. Energy Combust. Sci. 61, 189–248.
Silva, I.M., Dionisi, D., 2020. Effect of the operating conditions on the anaerobic digestion of wheatgrass for chemicals and energy production. Biomass Conver. Biorefinery 1–12.
Sun, S., He, S., Wu, C.J.C.E.J., 2022. Ni promoted Fe-CaO dual functional materials for calcium chemical dual looping, 441, 135752.
Tournier, V., Topham, C., Gilles, A., David, B., Folgoas, C., Moya-Leclair, E., Kamionka, E., Desrousseaux, M.-L., Texier, H., Gavalda, S., 2020. An engineered PET depolymerase to break down and recycle plastic bottles. Nat. Commun. 580, 216–219.
Villarrubia-Gómez, P., Carney Almroth, B., Cornell, S.E., 2022. *Re*-framing plastics pollution to include social, ecological and policy perspectives. Nat. Rev. Earth Environ. Sci. Technol. 3, 724–725.
Wang, Y., Memon, M.Z., Seelro, M.A., Fu, W., Gao, Y., Dong, Y. Ji, G.J.I.J.o.H.E., 2021. A review of CO2 sorbents for promoting hydrogen production in the sorption-enhanced steam reforming process, 46, 23358–23379.
Wang, Y., Memon, M.Z., Xie, Q., Gao, Y., Li, A., Fu, W., Wu, Z., Dong, Y., Ji, G.J.C.C.S., 2022. Study on CO2 sorption performance and sorption kinetics of Ce-and Zr-doped CaO-based sorbents. Technol. (Singap World Sci) 2, 100033.
Williams, P.T., 2021. Hydrogen and carbon nanotubes from pyrolysis-catalysis of waste plastics: a review. Waste BioMass Valorization. 12, 1–28.
Wu, C., Huang, Q., Xu, Z., Sipra, A.T., Gao, N., de Souza Vandenberghe, L.P., Vieira, S., Soccol, C.R., Zhao, R., Deng, S., 2024. A comprehensive review of carbon capture science and technologies. Carbon Capture Sci. Technol. 11, 100178.
Wu, C., Williams, P.T., 2009. Investigation of Ni-Al, Ni-Mg-Al and Ni-Cu-Al catalyst for hydrogen production from pyrolysis–gasification of polypropylene. Appl. Catal. B: Environ. 90, 147–156.
Wu, C., Williams, P.T., 2010. Investigation of coke formation on Ni-Mg-Al catalyst for hydrogen production from the catalytic steam pyrolysis-gasification of polypropylene. Appl. Catal. B: Environ. 96, 198–207.
Wu, S.-L., Kuo, J.-H., Wey, M.-Y., 2019. Thermal degradation of waste plastics in a two-stage pyrolysis-catalysis reactor over core-shell type catalyst. J. Anal. Appl. Pyrolysis 142, 104641.
Xu, D., Lu, X., Zhang, Y., Shearing, P.R., Zhang, S., Brett, D.J., Wang, S., 2022. Insights into in-situ catalytic degradation of plastic wastes over zeolite-based catalyst from perspective of three-dimensional pore structure evolution. Chem. Eng. J. 450, 138402.
Xu, D., Shen, C., Liu, X., Xie, W., Ding, H., Widenmeyer, M., Mellin, M., Qu, F., Rashid, A., Chen, G., 2023. Efficient transformation of plastic wastes to H2 and electromagnetic nanocarbon absorbents over molecular-level engineered 3D NiCo/MnO. Chem. Eng. J. 476, 146477.
Xu, Y., Tijssen, K.C., Bomans, P.H., Akiva, A., Friedrich, H., Kentgens, A.P., Sommerdijk, N.A., 2018. Microscopic structure of the polymer-induced liquid precursor for calcium carbonate. Nat. Commun. 9, 2582.
Zhang, S., Zhu, S., Zhang, H., Liu, X., Xiong, Y., 2019. High quality H2-rich syngas production from pyrolysis-gasification of biomass and plastic wastes by Ni–Fe@ nanofibers/porous carbon catalyst. Int. J. Hydrogen. Energy 44, 26193–26203.
Zhang, Y., Huang, J., Williams, P.T., 2017. Fe–Ni–MCM-41 catalysts for hydrogen-rich syngas production from waste plastics by pyrolysis–catalytic steam reforming. Energy Fuels. 31, 8497–8504.
Zhang, Y., Nahil, M.A., Wu, C., Williams, P.T., 2017. Pyrolysis–catalysis of waste plastic using a nickel–stainless-steel mesh catalyst for high-value carbon products. Environ. Technol. 38, 2889–2897.
Zhang, Y., Tao, Y., Huang, J., Williams, P.T., 2017. Influence of silica–alumina support ratio on H2 production and catalyst carbon deposition from the Ni-catalytic pyrolysis/reforming of waste tyres. Waste Manag. Res. 35, 1045–1054.
Zhang, Y., Williams, P.T., 2016. Carbon nanotubes and hydrogen production from the pyrolysis catalysis or catalytic-steam reforming of waste tyres. J. Anal. Appl. Pyrolysis 122, 490–501.
Zhang, Y., Wu, C., Nahil, M.A., Williams, P.T., 2015. Pyrolysis–catalytic reforming/gasification of waste tires for production of carbon nanotubes and hydrogen. Energy Fuels. 29, 3328–3334.
Zhang, Y., Zhu, H., Zhang, R., Yu, L., Liu, Z., Shearing, P.R., Brett, D.J., Williams, P.T., 2022. Study of tire pyrolysis oil model compound structure on carbon nanomaterial production. ACS Sustain. Chem. Eng. 10, 800–809.
Zhang, Y.S., Zhu, H.L., Yao, D., Williams, P.T., Wu, C., Xu, D., Hu, Q., Manos, G., Yu, L., Zhao, M., 2021. Thermo-chemical conversion of carbonaceous wastes for CNT and hydrogen production: a review. Sustain. Energy Fuels 5, 4173–4208.
Zhou, D., Wang, Y., Zhang, Z., Zhang, Y., Li, A., Luan, J., Ji, G.J.C.C.S., 2024. Vacuum assisted desorption of sodium zirconate sorbent for enhancing cyclic stability in pre–combustion CO2 capture. Technol. (Singap World Sci) 13, 100277.
Zhu, H.L., Zhang, Y.S., Materazzi, M., Aranda, G., Brett, D.J., Shearing, P.R., Manos, G., 2019. Co-gasification of beech-wood and polyethylene in a fluidized-bed reactor. Fuel Process. Technol. 190, 29–37.
Zou, S., Dong, W., Cheng, B., Zhang, Y., Williams, P.T., Zhao, M., 2021. Hybrid-functional material for sorption-enhanced hydrogen-rich syngas production from biomass: effect of material preparation process. BioMass BioEnergy 144, 105886.